BNL-224591-2023-JAAM

Improving Oxygen Reduction Performance of Surface-Layer-Controlled Pt-Ni Nano-Octahedra via Gaseous Etching

C. Li, L. Zhang

To be published in "Nano Letters"

April 2023

Center for Functional Nanomaterials

Brookhaven National Laboratory

U.S. Department of Energy

USDOE Office of Science (SC), Basic Energy Sciences (BES) (SC-22)

DISCLAIMER

Improving Oxygen Reduction Performance of Surface-Layer-Controlled Pt-Ni Nano-Octahedra *via* Gaseous Etching

Can Li,[1]† Soonho Kwon,[2]† Xiaobo Chen,[3]† Lihua Zhang,[4] Anju Sharma,[5] Shaojie Jiang,[1] Hanlei Zhang,[6] Ming Zhou,[1] Jinfong Pan,[1] Guangwen Zhou,[3] William A. Goddard III[2*] and Jiye Fang[1*]

[1]Department of Chemistry, State University of New York at Binghamton, Binghamton, New York 13902, United States;

[2]Materials and Process Simulation Center, California Institute of Technology, Pasadena, California 91125, United States;

[3]Materials Science and Engineering Program, Department of Mechanical Engineering, State University of New York at Binghamton, Binghamton, New York 13902, United States;

[4]Center for Functional Nanomaterials, Brookhaven National Laboratory, Upton, New York 11973, United States;

[5]Analytical and Diagnostics Lab, State University of New York at Binghamton, Binghamton, New York 13902, United States.

[6]Advanced Materials Characterization Laboratory, Materials Research Center, Missouri University of Science and Technology, Rolla, Missouri 65409, United States

*Corresponding authors. Emails: wag@caltech.edu; jfang@binghamton.edu
†These authors contributed equally to this work

ABSTRACT

This study demonstrates an atomic composition manipulation on Pt-Ni nano-octahedra to enhance their electrocatalytic performance. By selectively extracting Ni atoms from the {111} facets of the Pt-Ni nano-octahedra using gaseous carbon monoxide at an elevated temperature, a Pt-rich shell is formed, resulting in a ~2 atomic layer Pt-skin. The surface-engineered octahedral nanocatalyst exhibits a significant enhancement in both mass activity (~1.8-fold) and specific activity (~2.2-fold) toward the oxygen reduction reaction compared with its unmodified counterpart. After 20,000 potential cycles of durability tests, the surface-etched Pt-Ni nano-octahedral sample shows a mass activity of 1.50 A/mg_{Pt}, exceeding the initial mass activity of the unetched counterpart (1.40 A/mg_{Pt}) and outperforming the benchmark Pt/C (0.18 A/mg_{Pt}) by a factor of 8. DFT calculations predict this improvement with the Pt surface layers and support these experimental observations. This surface-engineering protocol provides a promising strategy for developing novel electrocatalysts with improved catalytic features.

Keywords: *gaseous etching, oxygen reduction reaction, Pt_3Ni nano-octahedron, Pt-shell {111} facets; deep learning.*

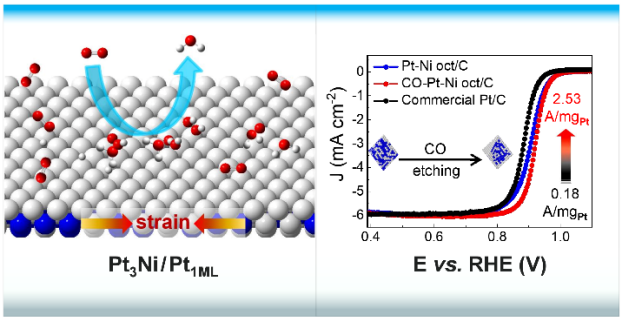

Platinum (Pt)-based nanocrystals (NCs) constitute a class of most promising catalysts for electrochemical reactions in green energy conversion devices, such as the oxygen reduction reaction (ORR) at the cathode of fuel cells.[1-5] To reduce the utilization of the precious Pt element and to enhance the ORR performance, many strategies have been demonstrated, such as alloying a 3*d* transition metal into the Pt lattice to provide a ligand effect that shifts the Pt *d*-band center, engineering the NC morphology to control the surface atomic arrangement on the desired facet, and developing a core-shell structure with a Pt-rich surface in the presence of strain effects.[6-17] Among these efforts, it has been reported that Pt_3Ni-based octahedral nanocatalysts containing exclusive {111} facets exhibit promising performance toward ORR.[18-30] Since it was determined that extended single crystal surfaces of $Pt_3Ni(111)$ exhibited an enhanced ORR activity that is 10-fold higher than Pt(111) and 90-fold higher than the current state-of-the-art Pt/C catalysts,[20] we have developed a wet-chemical synthesis approach in the presence of tungsten carbonyl [$W(CO)_6$] to successfully "transfer" exclusive and well-preserved {111} facets to the nanophase of Pt_3Ni.[18] The Pt_3Ni nano-octahedra produced from this synthesis strategy show superior ORR activity, demonstrating 64-times enhancement (octahedral $Pt_{2.5}Ni$/C *vs.* benchmark Pt/C) after acidic treatment.[19, 27] Nevertheless, these Pt-Ni catalysts face a stability challenge due to the potential Ni-leaching in acidic environments. Various surface engineering efforts, including the doping of a third transition metal (such as Co,[22] Ga,[31] Mo,[32-33] or Rh[24]) to Pt-Ni lattice, have been made to address this issue. We have developed an alternative protocol for dealloying of the Ni-component from $PtNi_4$ tetrahexahedral (THH) NCs through a carbon monoxide (CO) gaseous etching process in which most of the surface Ni atoms were pre-extracted by CO, being removed *via* producing $Ni(CO)_4$ gaseous product at an elevated temperature. This results in Pt_3Ni THH nanoframes with a Pt-rich layer on the outmost layers.[34] After removal of Ni with surface structure control in this novel process, the segregated compressively strained Pt layers on the 3D-nanoframes showed a downshifted *d*-band center, efficiently facilitating electrochemical reactions with demonstrated improved catalytic performance toward ORR and formic acid oxidation in acidic solutions.

In this study, we apply the CO gaseous etching approach to octahedral Pt_3Ni NCs, one class of the most viable electrocatalysts for ORR. We anticipated that a Pt-rich atomic shell could be created on the Pt-Ni octahedra with well-preserved Pt_3Ni (111) facets after this surface engineering of Ni dealloying using CO gas, from which improvement in durability and activity toward ORR is expected. Major steps for preparing the surface-engineered Pt-Ni octahedra/C catalyst are summarized in Scheme 1 in Supporting Information. Typical high-angle annular dark-field scanning transmission electron microscopic (HAADF-STEM) and transmission electron microscopic (TEM) images of the {111} face-terminated Pt-Ni nano-octahedra with uniform size and shape are shown in Figure S1. These NCs were subsequently loaded onto carbon black and designated as "Pt-Ni oct/C" (Figure S2). Next, a CO-etching process was carried out to manipulate

their surface structure, generating surface-engineered Pt-Ni octahedral electrocatalysts (designated as "CO-Pt-Ni oct/C").

Figure 1a shows a zoom-out TEM view of the as-synthesized monodisperse Pt-Ni nano-octahedra. Their average edge length was determined as 9.5 ± 0.8 nm with a reasonably narrow size distribution based on a direct measurement of ~100 randomly selected [110]-oriented nano-octahedra from a HAADF-STEM image (Figure S3a-c). To consider the NC sampling in all orientations, the average edge length was further refined as 10.4 nm through a deep-learning algorithm (Mask R-CNN model) based on a size input from a 2D HAADF-STEM imaging area containing ~100 nano-octahedra with all of the four-type octahedral projections (Figure S3c-g). Figure 1b is the HAADF-STEM energy dispersive X-ray spectroscopic (EDX) line scan profile of a typical nano-octahedron for elements Pt (red) and Ni (green) along the arrow direction indicated in the inserted HAADF-STEM image, showing the element fractions in the NC. The HAADF-STEM image (Figure 1c) taken from an individual octahedron along the [011] zone axis exhibits a single-crystal structure with exposed (111) facets. The lattice spacing between the (111) crystallographic planes of the NC was measured as 2.24 Å. The inset in Figure 1c shows a diffractogram (fast Fourier transform) of the HAADF image, while the indexed spots correspond to the *fcc* (111) lattice plane,[20] showing its high crystallinity. Figure 1d panel illustrates HAADF-STEM EDX elemental maps of a Pt-Ni nano-octahedron (Pt/red, Ni/green). The EDX line scan (Figure 1b) and EDX mapping profiles (Figure 1d) suggest a uniform composition distribution throughout the entire NC, indicating simultaneous co-reduction of Pt- and Ni-precursors during the synthesis process. As shown in Table S1, the composition of the bulk octahedral Pt-Ni NCs was also determined using an inductively coupled plasma-optical emission spectrometer (ICP-OES) technique, showing that the Pt/Ni atomic ratio ($\boldsymbol{R}_{Pt/Ni}$ = 2.57, or Pt:Ni = 72:28) is consistent with the proportion measured by EDX elemental mapping ($\boldsymbol{R}_{Pt/Ni}$ = 2.57, or Pt:Ni = 72:28).

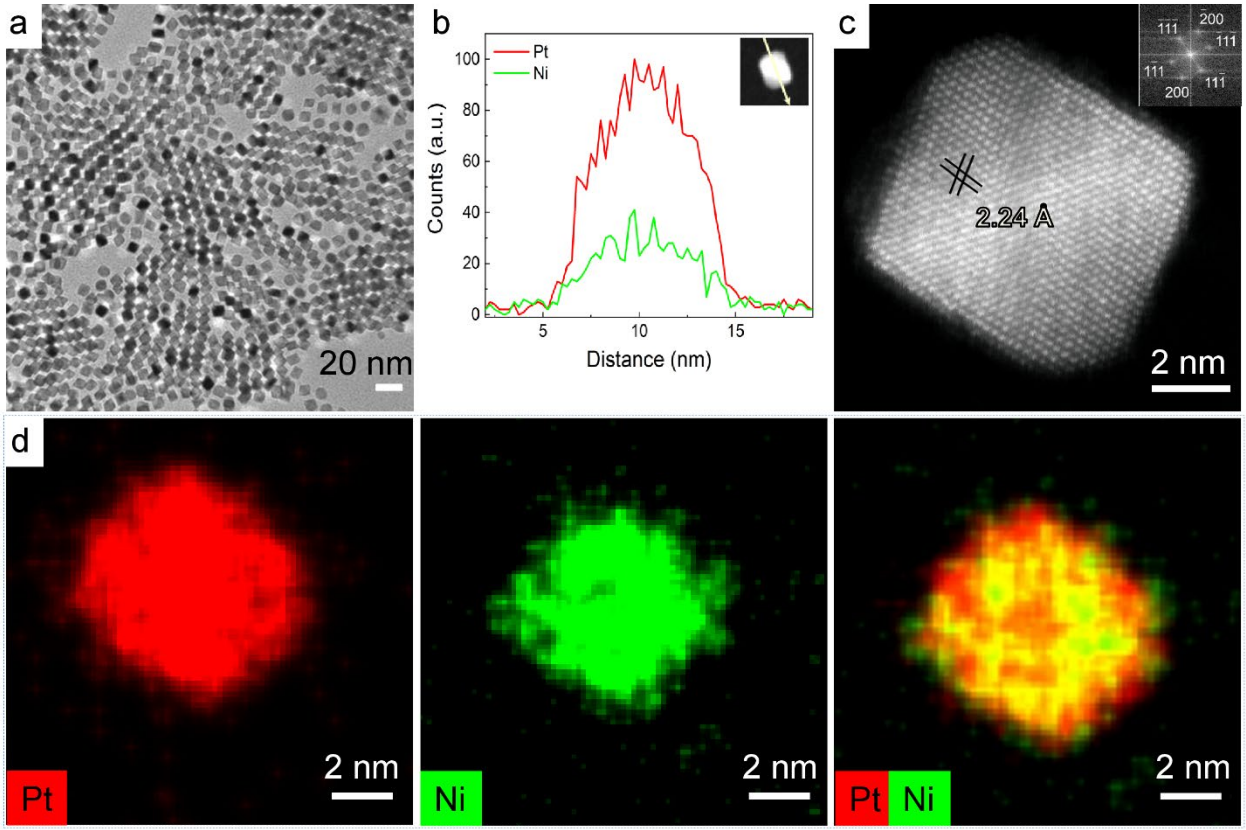

Figure 1. Characterization of the as-synthesized Pt-Ni octahedral NCs. (a) Typical TEM image of the Pt-Ni octahedra. (b) HAADF-STEM EDX line scan profile on an octahedron NC along the arrow-marked direction indicated in the inserted HAADF-STEM image. (c) HAADF-STEM high-resolution image of an octahedron in the zone axis of [110]; The inset in (c) is a diffractogram of the HAADF image. (d) HAADF-STEM EDX elemental maps of a representative octahedron (Pt/red, Ni/green), revealing spatial distributions of Pt and Ni atoms.

We report here similar analyses on CO-Pt-Ni oct/C. As shown in Figure 2a, the TEM image of the carbon-supported Pt-Ni NCs after the CO-etching indicates that the particles still preserve their octahedral morphology and are monodispersed with no aggregation. Figure 2b presents the EDX line-scan profiles of CO-Pt-Ni oct/C for Pt (red) and Ni (green) elements along the arrow direction indicated in the inserted HAADF-STEM image, showing a Pt-Ni@Pt core@shell structure with a thin Pt-shell layer (~0.5 nm, equivalent to ~2 atomic layers). The HAADF-STEM image shown in Figure 2c was taken from a typical individual CO-Pt-Ni oct/C NC along the [011] zone axis, demonstrating that the exposed (111) facets were well-preserved on the surfaces after the CO-etching treatment while the lattice spacing between the (111) crystallographic planes of the NC was not changed (2.24 Å). The diffractogram (shown in the inset of Figure 2c) also confirms the *fcc* structure, which is the same as for the untreated samples. The EDX maps (Figure 2d) show more Pt components in the outer layers of the octahedral NC compared with the Ni distribution, further verifying the core@shell structure generated during the CO-etching treatment. The composition of the CO-Pt-Ni oct/C sample was also analyzed using the ICP-OES technique, where the

Pt/Ni atomic ratio was determined as $\boldsymbol{R}_{Pt/Ni}$ = 2.85 (or Pt:Ni = 74:26), which is consistent with the outcome from the EDX elemental mapping ($\boldsymbol{R}_{Pt/Ni}$ = 2.70, or Pt:Ni = 73:27). These analysis results clearly suggest that some Ni atoms were effectively removed from the surface of the octahedral Pt-Ni NCs after this CO gaseous etching process.

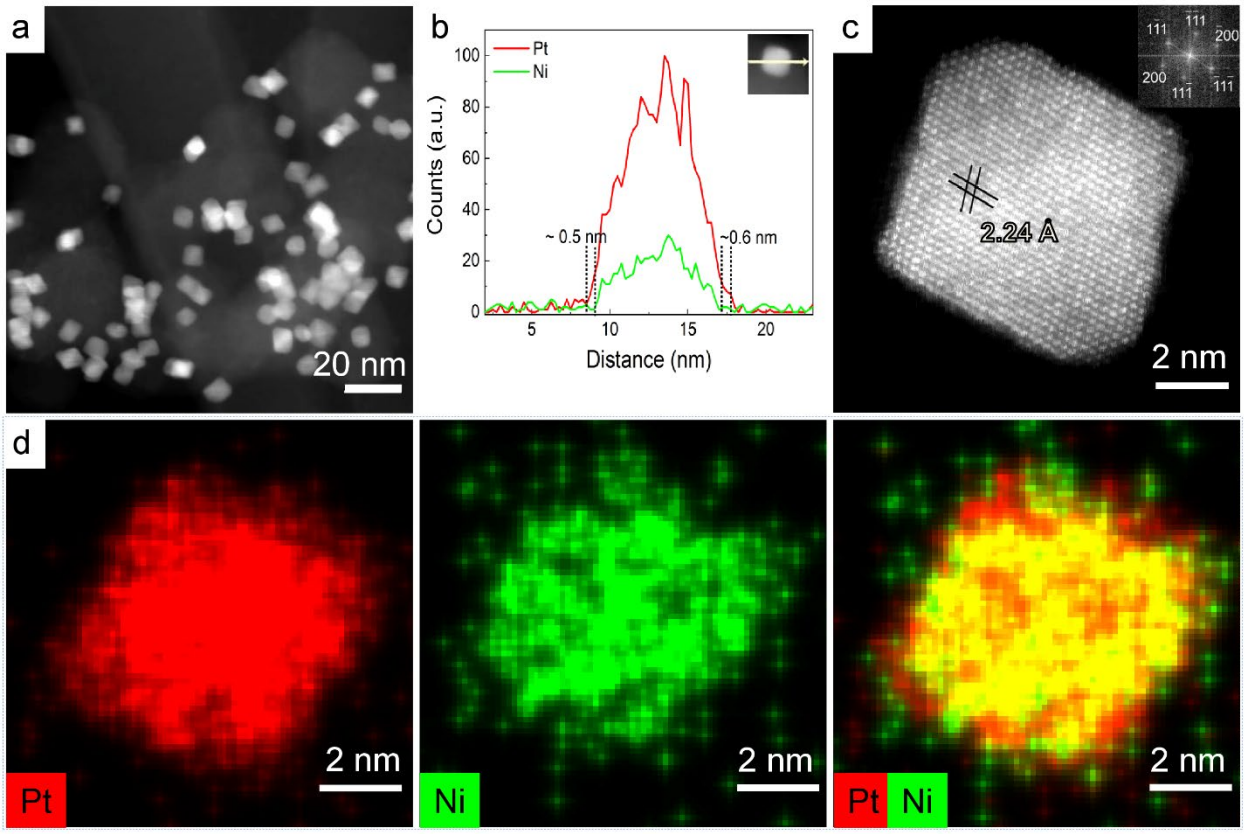

Figure 2. Characterization of the CO-Pt-Ni oct/C catalysts. (a) HAADF-STEM image of CO-Pt-Ni oct/C. (b) HAADF-STEM EDX line scan profile of a CO-Pt-Ni oct/C NC along the arrow direction indicated in the inserted HAADF-STEM image. (c) HAADF-STEM high-resolution image of an octahedron in the zone axis of [110]; The inset in (c) is a diffractogram of the HAADF image. (d) HAADF-STEM EDX elemental maps of a representative octahedron (Pt/red, Ni/green).

The phase structures of the aforementioned bulk Pt-Ni NCs were also investigated using Powder X-ray diffraction (XRD). As shown in Figure 3a, both octahedral Pt-Ni samples before and after the CO-etching treatment exhibit highly crystalline *fcc* structures of Pt_3Ni[16] with a right-shift of their diffraction peaks compared with the pure Pt XRD pattern (refer to JCPDS-ICDD card 04-0802) due to the incorporation of Ni atoms into the Pt lattice. Pawley fitting verifies the $Fm\bar{3}m$ symmetry on both Pt-Ni samples and also shows a slight increase of the unit cell parameter, *a*, after the CO-etching treatment (Figure S4), implying

the removal of Ni atoms. The reduction of the Ni fraction in CO-Pt-Ni oct/C is further confirmed by the left-shift of its diffraction peaks (*e.g.,* ~0.2 degrees in 2θ at (111) peak, Figure 3b) according to the Pawley fitting, implying extraction of Ni from the Pt-Ni NCs by the CO-etching and the possible presence of a Pt-rich surface on the octahedral NCs after CO-etching treatment.[3, 8] The X-ray photoelectron spectroscopic (XPS) technique was also used to identify possible changes in the electronic structure of the Pt-Ni NCs before and after the CO-etching treatment. The Pt 4*f* spectrum (Figure 3c) implies the dominance of zero-valent Pt in both the Pt-Ni oct/C and CO-Pt-Ni oct/C catalysts. Compared to the zero-valent Pt in pure Pt metal (71.0 eV), the binding energy of Pt 4*f* peaks in Pt-Ni oct/C increased by ~0.3 eV. A similar Pt 4*f* binding energy was also observed in the CO-Pt-Ni oct/C sample. On the other hand, the Ni 2*p* XPS spectrum of Pt-Ni oct/C (Figure 3d) shows signs of both Ni^{o} and Ni^{2+}, possibly due to the presence of $Ni(OH)_2$ from the surface oxidation of Ni. However, the Ni^{2+} signal was dramatically suppressed in the XPS spectrum of CO-Pt-Ni oct/C, indicating the absence of Ni^{2+} on the surface of the CO-treated sample. Combined with the TEM information, this result helps further understand the CO gaseous etching. In the reducing atmosphere at an elevated temperature, the oxidized Ni species on the NC surfaces should be reduced to metallic Ni. The zero-valent Ni further reacted with CO to form gaseous $Ni(CO)_4$ with subsequent removal from the NC surface by the CO stream, eventually generating a Pt(111) thin shell on the NC.[34] In addition, we recorded the W 4*f* spectrum (Figure S5). Unlike previous reports in which WO_x was detected from the product even though W does not incorporate into the lattice of Pt-Ni or Pt-Fe under the specified synthesis condition,[16, 27, 35] we did not detect W-species by XPS from both Pt-Ni oct/C and CO-Pt-Ni oct/C samples, indicating the effectiveness of the cleaning process used in this work. It is worth pointing out that the complete removal of W components from the NCs prior to the surface treatment is required to ensure the success of the surface engineering *via* the gaseous etching and their accurate comparison in terms of the ORR performance. In addition, $\boldsymbol{R}_{Pt/Ni}$ based on the XPS data shows the same trend of composition change before and after this CO-etching process, that is, $\boldsymbol{R}_{Pt/Ni}$ = 1.44 (or Pt:Ni = 59:41) *vs.* $\boldsymbol{R}_{Pt/Ni}$ = 2.13 (or Pt:Ni = 68:32), respectively. However, these XPS-based Pt/Ni atomic ratios are fairly far from the $\boldsymbol{R}_{Pt/Ni}$ determined from ICP-OES and EDX, exhibiting higher Ni fractions (Table S1). This could be due to the inhomogeneous distribution of Pt and Ni over the whole Pt-Ni octahedral NC as a random nano-alloy. During the NC synthesis, the Pt-precursors are easy to be reduced to Pt atoms for early nucleation ($E^{o}_{Pt^{2+}/Pt^{0}}$ = 1.18 V) compared with the Ni-precursors ($E^{o}_{Ni^{2+}/Ni^{0}}$ = - 0.257 V), leading to abundant Ni-components "segregated" on the upper mantle of the seeds. Unlike ICP and EDX analyses that correspond to the bulk contents, only the surface compositions are sensitive to XPS. This is also consistent with the fact that the XPS-determined nickel-loss-percentage (~22%) after the CO etching process, defined as (Ni at% $_{\text{before process}}$ - Ni at% $_{\text{after process}}$) / Ni at% $_{\text{before process}}$, is much higher than those measured by ICP-OES (~7%) and EDX (~4%).

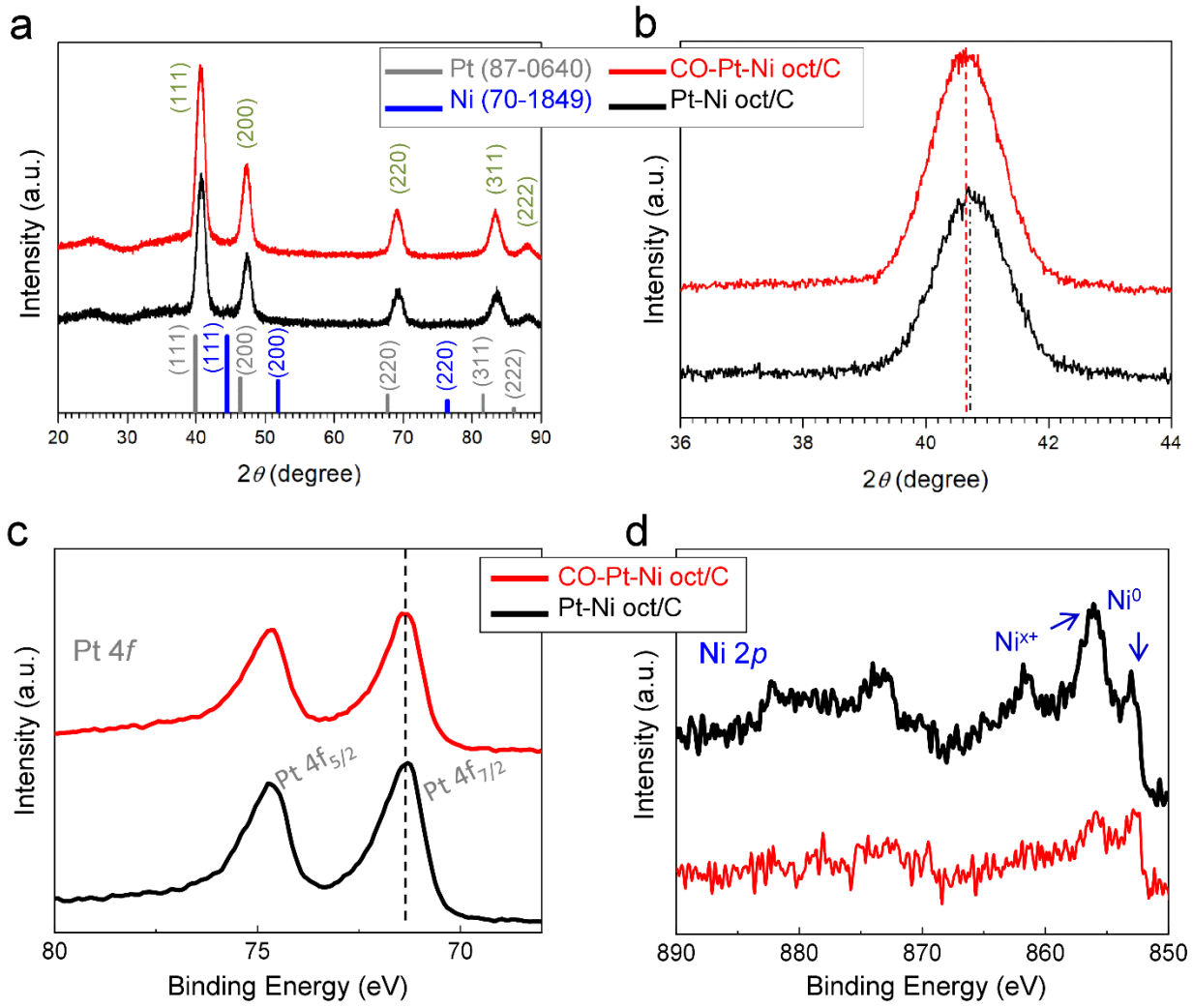

Figure 3. XRD and XPS characterizations of the octahedral Pt-Ni NCs before and after the CO-etching treatment. (a) and (b) XRD patterns of Pt-Ni oct/C (black) and CO-Pt-Ni oct/C (red) in a full-range scan and peak (111) scan, respectively. (c) and (d) XPS spectra of the Pt 4*f* and Ni 2*p*, respectively. The grey and blue lines on the bottom of (a) show standard XRD patterns of Pt and Ni (JCPDS-ICDD cards 87-0640 and 70-1849), respectively.

Figure 4a shows the anodic ORR polarization curves of the three samples. The CO-Pt-Ni oct/C exhibited a half-wave potential value ($E_{1/2}$) of 0.933 V *vs.* reversible hydrogen electrode (RHE), which is ~47 mV more positive than that of the Pt/C and ~12 mV more positive than that of Pt-Ni oct/C. The kinetic current was then calculated based on the Koutecky-Levich equation and normalized against the mass loading of Pt on the electrode or electrochemically active surface area (ECSA) at 0.90 V *vs.* RHE to calculate the mass activity (MA) or specific activity (SA), respectively. As illustrated in Figure 4b, the MA of CO-Pt-Ni oct/C was determined as 2.53 A/mg_{Pt}, which is ~1.8 times and ~14 times as high as that of Pt-Ni oct/C (1.40 A/mg_{Pt}) and the benchmark Pt/C (0.18 A/mg_{Pt}), respectively. The CO-Pt-Ni oct/C also

showed superior specific activity, and with a SA (6.02 mA/cm^2) that is ~2.2 times and ~23 times as high as that of Pt-Ni oct/C (2.75 mA/cm^2) and the benchmark Pt/C (0.26 mA/cm^2), respectively.

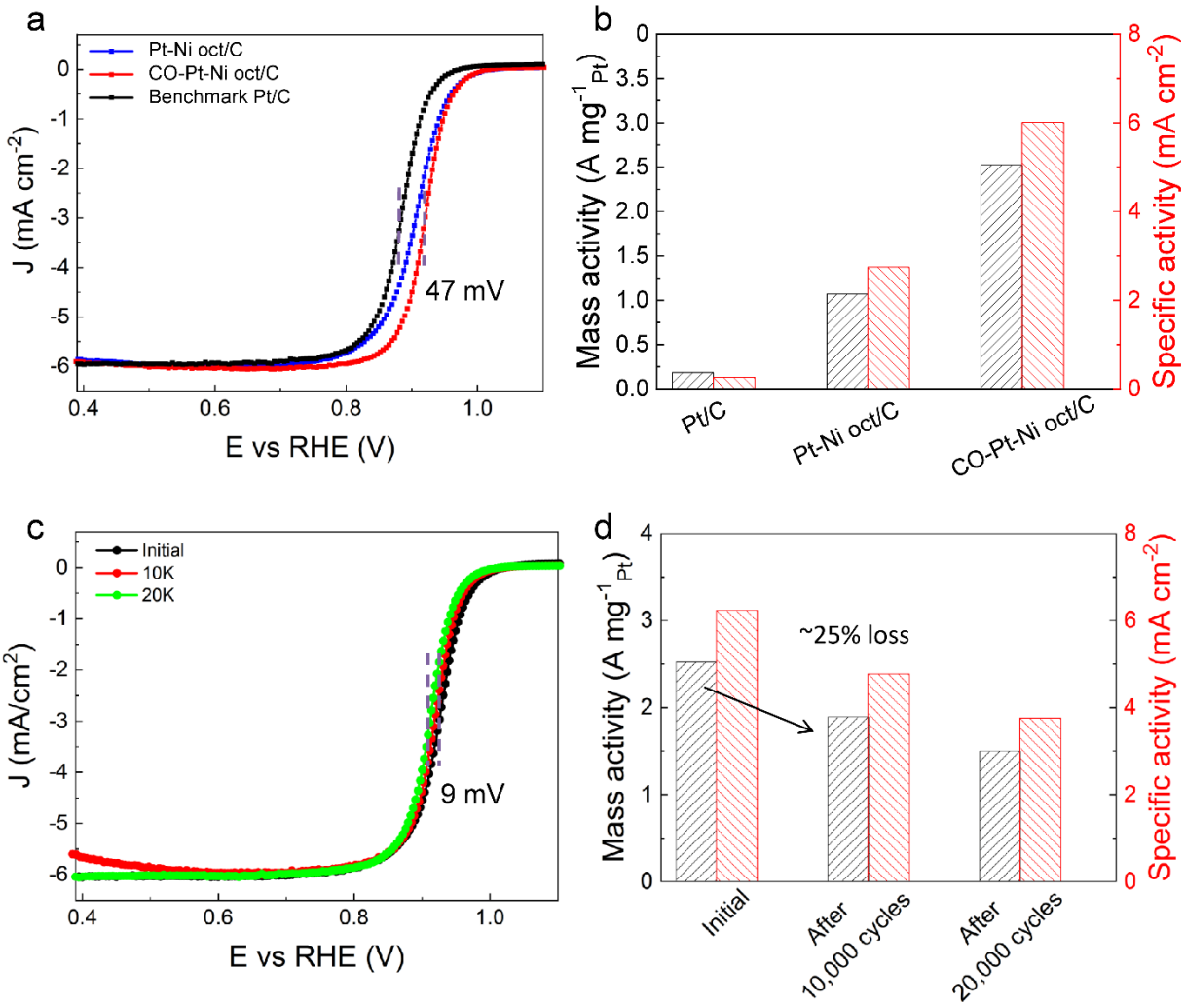

Figure 4. Electrocatalytic properties of the Pt-Ni oct/C, CO-Pt-Ni oct/C, and benchmark Pt/C. (a) ORR polarization curves recorded in O_2-saturated 0.1 M $HClO_4$ solutions with a potential scan rate of 5 mV/s and an electrode rotation speed of 1,600 rpm. (b) mass and specific activities at 0.9 V *vs.* RHE. (c) ORR polarization curves of the CO-Pt-Ni oct/C catalyst before and after durability tests in O_2-saturated 0.1 M $HClO_4$ at 1,600 rpm and a scan rate of 5 mV/s. (d) mass and specific activities of the CO-Pt-Ni oct/C catalyst at 0.9 V *vs.* RHE before and after durability tests.

The durability of the CO-Pt-Ni oct/C catalysts was further evaluated through accelerated durability tests (ADTs) by applying continuous potential cycling between 0.6 V and 1.0 V *vs.* RHE in O_2-saturated $HClO_4$ solution at room temperature. After 20,000 cycles of ADT, we observed a downshift of only ~9 mV (Figure 4c), demonstrating remarkable stability toward ORR. From the CV profiles (Figure S6) recorded every 10,000 potential cycles, we observed that the peak strength of adsorption and desorption of hydrogen

(H_{UPD}) decreased slightly, implying that surface area loss can explain the activity decrease of the as-achieved catalyst. As shown in Figure 4d, the MA of CO-Pt-Ni oct/C dropped to 1.90 A/mg_{Pt} after 10,000 potential cycles, and to 1.5A/mg_{Pt} after 20,000 potential cycles. But this still exceeds the initial mass activities of its unmodified counterpart and the benchmark Pt/C catalysts. Based on the TEM observations and corresponding EDX analysis (Figures S7, S8), the particles of CO-Pt-Ni oct/C became more truncated/spherical after the ADTs. Compared to the morphology before the durability test, the fractional decrease of the Pt-Ni(111) facet should be attributed to the loss of MA. Although the ICP-OED-based (or EDX-based) Pt/Ni molar ratio, $\boldsymbol{R}_{Pt/Ni}$, increased from 2.85 to 3.76 (or from 2.70 to 3.55) after the ADTs (20,000 potential cycles), showing a nickel-loss-percentage (defined above) of ~19% (based on either the ICP-OES or EDX data), it is apparent that more Ni contents are retained in CO-Pt-Ni oct/C by comparing the corresponding nickel-loss-percentage of the unetched sample (Pt-Ni oct/C, ~39 % from ICP-OES; ~36 % from EDX) based on the data provided in Table S1. The nickel-loss-percentage of CO-Pt-Ni oct/C is also lower than that reported previously.[19, 27] This advantage can be attributed to the more stable $Pt_3Ni/Pt_{1ML}/V_{Pt}$ surface structure in the CO-treated catalyst (*vide infra*).

To understand the correlation between the surface structure and ORR performance, we carried out Quantum Mechanics (QM) calculations (at the PBE-D3 flavor of DFT) using various $Pt_3Ni(111)$ surface models to study the effect of different compositions, configurations, and points defects (Figure S9).

- Pt_3Ni/Pt_{1ML} denotes a monolayer (ML) of pure Pt with a Pt_3Ni substrate,
- Pt_3Ni/Pt_{2ML} denotes two MLs of pure Pt with a Pt_3Ni substrate,
- $Pt_3Ni/Pt_{1.5ML}$ represents the model consisting of top Pt ML with a 1:1 atomic ratio of Ni/Pt in the first sublayer,[20]
- We also included pure Pt_3Ni and
- $Pt_3Ni/Pt_{1ML}/V_{Pt}$ which has 0.25 ML of Pt vacancies based on Pt_3Ni/Pt_{1ML} to mimic our Ni-leaching process.

The four-electron ORR pathway *via* peroxy intermediates is given by the elementary steps

(1) $O_{2(g)} + H^+ + e^- \leftrightarrow OOH^*$: $O_{2(g)}$ reduction

(2) $OOH^* + H^+ + e^- \leftrightarrow O^*$: OOH* reduction

(3) $O^* + H_2O_{(l)} \leftrightarrow 2OH^*$: O* hydrolysis

(4) $2 \times (OH^* H^+ + e^- \leftrightarrow H_2O_{(l)})$: Water formation

Based on QM metadynamics study using five layers of explicit solvent, Cheng et al.[36] showed that

- at a potential above 0.87 V *vs.* RHE, the rate-determining step (RDS) on Pt(111) is the electrochemical reduction of OH* to form water, step 4,
- at a potential below 0.87 V *vs.* RHE, the RDS is the nonelectrochemical surface oxygen (O*) hydrolysis to produce two OH*, step 3.

The ORR pathway and corresponding free energy diagram at 1.23 V *vs.* RHE are shown in Figure 5a. We found that the overpotential is determined by the OH* reduction (water formation) step 4 without exception. We calculated the overpotential of each (111) surface to be

- 0.63 V for pure Pt,
- 0.59 V for Pt_3Ni/Pt_{2ML},
- 0.61 V for Pt_3Ni/Pt_{1ML},
- 0.42 V for $Pt_3Ni/Pt_{1.5ML}$,
- 0.94 V for ($Pt_3Ni/Pt_{1ML}/V_{Pt}$), and
- 0.67 V for pure Pt_3Ni.

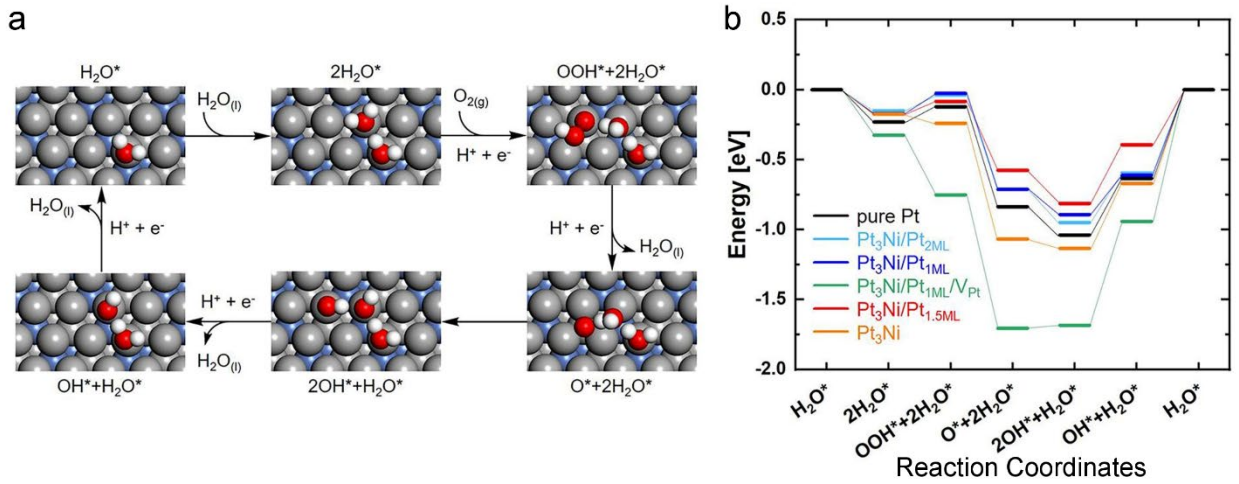

Figure 5. Surface models and Gibbs free energy diagram of Pt-Ni catalysts for ORR. (a) The four-electron ORR pathway; The white, red, grey, and blue spheres represent H, O, Pt, and Ni atoms, respectively. (b) Gibbs free energy diagram for the ORR pathway on various Pt-Ni surface models at 1.23 V *vs.* RHE.

Although $Pt_3Ni/Pt_{1.5ML}$ is the most active phase with 0.21 V lower overpotential compared to pure Pt, we note that the Pt_3Ni/Pt_{2ML} model has 0.04 V lower overpotential than pure Pt which is in line with the

~47 mV higher $E_{1/2}$ for CO-Pt-Ni oct/C compared to Pt/C. The Pt_3Ni/Pt_{2ML} also has 4.62 Å-thick pure Pt layers (2ML), which agrees with our EDX analysis (Figure 2b). This activity enhancement originates from the weaker binding of OH* on Pt, facilitating its reduction to water. The reaction free energy of O* hydrolysis does not depend significantly on the Ni incorporation in the sublayers (Table S2) confirming that the water formation step determines ORR activity. We found that the presence of vacancies ($Pt_3Ni/Pt_{1ML}/V_{Pt}$) induces stronger binding of all reaction intermediates leading to a high overpotential of 0.94 V while also making the O hydrolysis step endothermic (Figure 5b). Therefore, based on the high performance of our catalysts, we deduced that the surface of our catalyst is effectively cured to a clean Pt skin during the CO etching. Although the activity could be further enhanced by increasing the Ni ratio up to 50% in the first sublayer, strong interaction between surface oxygen and oxophilic Ni near the surface and the resulting Ni dissolution would likely perturb the surface Pt during ORR causing deterioration in performance. We conclude that the preparation of close-packed Pt 2MLs through CO-etching effectively prevents the Ni-O interaction, leading to the observed high durability for ORR.

In conclusion, we synthesized Pt-Ni nano-octahedra in an average edge length of ~9.5 nm (the deep-learning algorithm suggests 10.4 nm as the average edge length with a consideration of all four-type octahedral projections) and demonstrated the atomic manipulation of the surface composition of NCs *via* the CO gaseous etching process. During the CO-etching treatment at an elevated temperature, the octahedral morphology of Pt-Ni NCs was well preserved with {111} facets while a Pt-rich shell with ~2 atomic layers was generated through the extraction of Ni atoms. We showed that this unique nanostructure exhibits superior electrocatalytic activity toward ORR in acid media when compared with the octahedral Pt-Ni counterpart without the Pt-shell and the benchmark Pt/C. We further determined that the CO-treated octahedral Pt-Ni nanocatalysts delayed the decay in the ORR activity that might be caused by Ni leaching and morphology deformation and would occur in their unmodified counterpart and the benchmark Pt/C sooner. Our QM calculations confirmed that the model of two pure Pt monolayers on top of the Pt_3Ni substrate is the most consistent. Thus, this work provides a new platform to improve Pt-Ni-based ORR catalysts. Moreover, this gaseous etching protocol could be extended to other types of electrocatalyst development to further maximize their ORR performance.

ASSOCIATED CONTENT

*** Supporting Information**

The Supporting Information is available free of charge at https://pubs.acs.org/doi/10.1021/acs.nanolett.xxxx.

- Experimental method and computation method, schematic illustration of sample preparation procedure, HAADF-STEM and TEM images and size (edge length) determination of the as-prepared octahedral Pt-Ni NCs, TEM image of carbon-supported octahedral Pt-Ni NCs, lattice parameters of CO-Pt-Ni oct/C and Pt-Ni oct/C received from Pawley fitting, CV curves of CO-Pt-Ni oct/C catalysts before and after the accelerated durability tests, EM images and EDX maps/line-scan profile of CO-Pt-Ni oct/C after the accelerated durability tests, additional XPS, electrochemical measurements, and DFT results (PDF)

AUTHOR INFORMATION

Corresponding Authors

William A. Goddard III - Materials and Process Simulation Center, California Institute of Technology, Pasadena, California 91125, United States. orcid.org/0000-0003-0097-5716; Email: wag@caltech.edu
Jiye Fang - Department of Chemistry, State University of New York at Binghamton, Binghamton, New York 13902, United States. orcid.org/0000-0003-3703-3204; Email: jfang@binghamton.edu

Authors

Can Li - Department of Chemistry, State University of New York at Binghamton, Binghamton, New York 13902, United States. orcid.org/0000-0001-8894-5110.
Soonho Kwon - Materials and Process Simulation Center, California Institute of Technology, Pasadena, California 91125, United States. orcid.org/0000-0002-9225-3018
Xiaobo Chen - Materials Science and Engineering Program, Department of Mechanical Engineering, State University of New York at Binghamton, Binghamton, New York 13902, United States. orcid.org/0000-0003-2943-2926
Lihua Zhang - Center for Functional Nanomaterials, Brookhaven National Laboratory, Upton, New York 11973, United States. orcid.org/0000-0003-3331-2345
Anju Sharma - Analytical and Diagnostics Lab, State University of New York at Binghamton, Binghamton, New York 13902, United States.
Shaojie Jiang - Department of Chemistry, State University of New York at Binghamton, Binghamton, New York 13902, United States. orcid.org/0000-0001-8692-0673
Hanlei Zhang - Advanced Materials Characterization Laboratory, Materials Research Center, Missouri University of Science and Technology, Rolla, MO 65409, United States. orcid.org/0000-0001-6540-0556
Ming Zhou - Department of Chemistry, State University of New York at Binghamton, Binghamton, New York 13902, United States. orcid.org/0000-0002-2708-0501
Jinfong Pan - Department of Chemistry, State University of New York at Binghamton, Binghamton, New York 13902, United States. orcid.org/ 0000-0001-8106-0678
Guangwen Zhou - Materials Science and Engineering Program, Department of Mechanical Engineering, State University of New York at Binghamton, Binghamton, New York 13902, United States. orcid.org/0000-0002-9243-293X

AUTHOR CONTRIBUTIONS

†C.L., S.K., and X.C. contributed equally to this work.

Notes

The authors declare no competing financial interest.

ACKNOWLEDGMENTS

This work was primarily supported by the National Science Foundation (NSF) under grant DMR-1808383. The theoretical work used the Extreme Science and Engineering Discovery Environment (XSEDE) for DFT calculations, which is supported by the NSF under grant ACI-1548562. W.A.G. thanks the support by the NSF (CBET-2005250, program manager: Bob McCabe), S.K. acknowledges support from the Resnick Sustainability Institute at Caltech; X.C. and G.Z. are thankful for the financial support by the NSF under grant DMR-1905422. L.Z. acknowledges the use of TEM facilities for the structural characterizations, at the Center for Functional Nanomaterials, Brookhaven National Laboratory, which is supported by the U.S. DOE, Office of Science, Basic Energy Sciences under grant DE-SC0012704. Partial low-magnification TEM imaging work was supported by S3IP/ADL, the State University of New York at Binghamton.

REFERENCES

1. Zhou, M.; Li, C.; Fang, J. Noble-Metal Based Random Alloy and Intermetallic Nanocrystals: Syntheses and Applications. *Chem. Rev.* **2021,** *121* (2), 736-795.

2. Shi, Y.; Lyu, Z.; Zhao, M.; Chen, R.; Nguyen, Q. N.; Xia, Y. Noble-Metal Nanocrystals with Controlled Shapes for Catalytic and Electrocatalytic Applications. *Chem. Rev.* **2021,** *121* (2), 649-735.

3. Li, C.; Yan, S.; Fang, J. Construction of Lattice Strain in Bimetallic Nanostructures and Its Effectiveness in Electrochemical Applications. *Small* **2021,** *17* (46), 2102244.

4. Gilroy, K. D.; Ruditskiy, A.; Peng, H. C.; Qin, D.; Xia, Y. Bimetallic Nanocrystals: Syntheses, Properties, and Applications. *Chem. Rev.* **2016,** *116* (18), 10414-72.

5. Stamenkovic, V. R.; Strmcnik, D.; Lopes, P. P.; Markovic, N. M. Energy and Fuels from Electrochemical Interfaces. *Nat. Mater.* **2016,** *16* (1), 57-69.

6. Li, C.; Chen, X.; Zhang, L.; Yan, S.; Sharma, A.; Zhao, B.; Kumbhar, A.; Zhou, G.; Fang, J. Synthesis of Core@Shell Cu-Ni@Pt-Cu Nano-Octahedra and Their Improved MOR Activity. *Angew. Chem. Int. Ed.* **2021,** *60* (14), 7675-7680.

7. Zhu, Y.; Peng, J.; Zhu, X.; Bu, L.; Shao, Q.; Pao, C. W.; Hu, Z.; Li, Y.; Wu, J.; Huang, X. A Large-Scalable, Surfactant-Free, and Ultrastable Ru-Doped Pt_3Co Oxygen Reduction Catalyst. *Nano Lett.* **2021,** *21* (15), 6625-6632.

8. Xie, M.; Lyu, Z.; Chen, R.; Shen, M.; Cao, Z.; Xia, Y. Pt-Co@Pt Octahedral Nanocrystals: Enhancing Their Activity and Durability toward Oxygen Reduction with an Intermetallic Core and an Ultrathin Shell. *J. Am. Chem. Soc.* **2021,** *143* (22), 8509-8518.

9. Xiao, W.; Lei, W.; Gong, M.; Xin, H. L.; Wang, D. Recent Advances of Structurally Ordered Intermetallic Nanoparticles for Electrocatalysis. *ACS Catal.* **2018,** *8* (4), 3237-3256.

10. Zhao, X. R.; Xi, C.; Zhang, R.; Song, L.; Wang, C. Y.; Spendelow, J. S.; Frenkel, A. I.; Yang, J.; Xin, H. L.; Sasaki, K. High-Performance Nitrogen-Doped Intermetallic PtNi Catalyst for the Oxygen Reduction Reaction. *ACS Catal.* **2020,** *10* (18), 10637-10645.

11. Kim, C.; Dionigi, F.; Beermann, V.; Wang, X.; Moller, T.; Strasser, P. Alloy Nanocatalysts for the Electrochemical Oxygen Reduction (ORR) and the Direct Electrochemical Carbon Dioxide Reduction Reaction (CO_2RR). *Adv. Mater.* **2019,** *31* (31), e1805617.

12. Li, J.; Xi, Z.; Pan, Y. T.; Spendelow, J. S.; Duchesne, P. N.; Su, D.; Li, Q.; Yu, C.; Yin, Z.; Shen, B.; Kim, Y. S.; Zhang, P.; Sun, S. Fe Stabilization by Intermetallic $L1_0$-FePt and Pt Catalysis Enhancement in $L1_0$-FePt/Pt Nanoparticles for Efficient Oxygen Reduction Reaction in Fuel Cells. *J. Am. Chem. Soc.* **2018,** *140* (8), 2926-2932.

13. Xiong, Y.; Xiao, L.; Yang, Y.; DiSalvo, F. J.; Abruña, H. D. High-Loading Intermetallic Pt_3Co/C Core–Shell Nanoparticles as Enhanced Activity Electrocatalysts toward the Oxygen Reduction Reaction (ORR). *Chem. Mater.* **2018,** *30* (5), 1532-1539.

14. Wang, C.; Lin, C.; Zhang, L.; Quan, Z.; Sun, K.; Zhao, B.; Wang, F.; Porter, N.; Wang, Y.; Fang, J. Pt_3Co Concave Nanocubes: Synthesis, Formation Understanding, and Enhanced Catalytic Activity toward Hydrogenation of Styrene. *Chem. Eur. J.* **2014,** *20* (6), 1753-9.

15. Strasser, P.; Koh, S.; Anniyev, T.; Greeley, J.; More, K.; Yu, C.; Liu, Z.; Kaya, S.; Nordlund, D.; Ogasawara, H.; Toney, M. F.; Nilsson, A. Lattice-Strain Control of the Activity in Dealloyed Core–Shell Fuel Cell Catalysts. *Nat. Chem.* **2010,** *2*, 454.

16. Zhang, J.; Fang, J. A General Strategy for Preparation of Pt 3d-Transition Metal (Co, Fe, Ni) Nanocubes. *J. Am. Chem. Soc.* **2009,** *131* (51), 18543-7.

17. Stamenkovic, V. R.; Mun, B. S.; Arenz, M.; Mayrhofer, K. J.; Lucas, C. A.; Wang, G.; Ross, P. N.; Markovic, N. M. Trends in Electrocatalysis on Extended and Nanoscale Pt-Bimetallic Alloy Surfaces. *Nat. Mater.* **2007,** *6* (3), 241-7.

18. Zhang, J.; Yang, H.; Fang, J.; Zou, S. Synthesis and Oxygen Reduction Activity of Shape-Controlled Pt_3Ni Nanopolyhedra. *Nano Lett.* **2010,** *10* (2), 638-44.

19. Choi, S.-I.; Xie, S.; Shao, M.; Odell, J. H.; Lu, N.; Peng, H.-C.; Protsailo, L.; Guerrero, S.; Park, J.; Xia, X.; Wang, J.; Kim, M. J.; Xia, Y. Synthesis and Characterization of 9 nm Pt–Ni Octahedra with a Record High Activity of 3.3 A/mgPt for the Oxygen Reduction Reaction. *Nano Lett.* **2013,** *13* (7), 3420-3425.

20. Stamenkovic, V. R.; Fowler, B.; Mun, B. S.; Wang, G.; Ross, P. N.; Lucas, C. A.; Markovic, N. M. Improved Oxygen Reduction Activity on $Pt_3Ni(111)$ via Increased Surface Site Availability. *Science* **2007,** *315* (5811), 493-497.

21. Chen, C.; Kang, Y.; Huo, Z.; Zhu, Z.; Huang, W.; Xin, H. L.; Snyder, J. D.; Li, D.; Herron, J. A.; Mavrikakis, M.; Chi, M.; More, K. L.; Li, Y.; Markovic, N. M.; Somorjai, G. A.; Yang, P.; Stamenkovic, V. R. Highly Crystalline Multimetallic Nanoframes with Three-Dimensional Electrocatalytic Surfaces. *Science* **2014,** *343* (6177), 1339-43.

22. Huang, X. Q.; Zhao, Z. P.; Chen, Y.; Zhu, E. B.; Li, M. F.; Duan, X. F.; Huang, Y. A Rational Design of Carbon-Supported Dispersive Pt-Based Octahedra as Efficient Oxygen Reduction Reaction Catalysts. *Energy Environ. Sci.* **2014,** *7* (9), 2957-2962.

23. Huang, X.; Zhao, Z.; Cao, L.; Chen, Y.; Zhu, E.; Lin, Z.; Li, M.; Yan, A.; Zettl, A.; Wang, Y. M.; Duan, X.; Mueller, T.; Huang, Y. High-Performance Transition Metal-Doped Pt_3Ni Octahedra for Oxygen Reduction Reaction. *Science* **2015,** *348* (6240), 1230-4.

24. Beermann, V.; Gocyla, M.; Willinger, E.; Rudi, S.; Heggen, M.; Dunin-Borkowski, R. E.; Willinger, M. G.; Strasser, P. Rh-Doped Pt-Ni Octahedral Nanoparticles: Understanding the Correlation between Elemental Distribution, Oxygen Reduction Reaction, and Shape Stability. *Nano Lett.* **2016,** *16* (3), 1719-25.

25. Kong, F.; Ren, Z.; Norouzi Banis, M.; Du, L.; Zhou, X.; Chen, G.; Zhang, L.; Li, J.; Wang, S.; Li, M.; Doyle-Davis, K.; Ma, Y.; Li, R.; Young, A.; Yang, L.; Markiewicz, M.; Tong, Y.; Yin, G.; Du, C.; Luo, J.; Sun, X. Active and Stable Pt–Ni Alloy Octahedra Catalyst for Oxygen Reduction via Near-Surface Atomical Engineering. *ACS Catal.* **2020,** *10* (7), 4205-4214.

26. Xiao, F.; Qin, X.; Xu, M.; Zhu, S.; Zhang, L.; Hong, Y.; Choi, S.-I.; Chang, Q.; Xu, Y.; Pan, X.; Shao, M. Impact of Heat Treatment on the Electrochemical Properties of Carbon-Supported Octahedral Pt–Ni Nanoparticles. *ACS Catal.* **2019,** *9* (12), 11189-11198.

27. Niu, G.; Zhou, M.; Yang, X.; Park, J.; Lu, N.; Wang, J.; Kim, M. J.; Wang, L.; Xia, Y. Synthesis of Pt-Ni Octahedra in Continuous-Flow Droplet Reactors for the Scalable Production of Highly Active Catalysts toward Oxygen Reduction. *Nano Lett.* **2016,** *16* (6), 3850-7.

28. Wu, Y.; Cai, S.; Wang, D.; He, W.; Li, Y. Syntheses of Water-Soluble Octahedral, Truncated Octahedral, and Cubic Pt-Ni Nanocrystals and Their Structure-Activity Study in Model Hydrogenation Reactions. *J. Am. Chem. Soc.* **2012,** *134* (21), 8975-81.

29. Gan, L.; Cui, C.; Heggen, M.; Dionigi, F.; Rudi, S.; Strasser, P. Element-Specific Anisotropic Growth of Shaped Platinum Alloy Nanocrystals. *Science* **2014,** *346* (6216), 1502-6.

30. Becknell, N.; Son, Y.; Kim, D.; Li, D.; Yu, Y.; Niu, Z.; Lei, T.; Sneed, B. T.; More, K. L.; Markovic, N. M.; Stamenkovic, V. R.; Yang, P. Control of Architecture in Rhombic Dodecahedral Pt-Ni Nanoframe Electrocatalysts. *J. Am. Chem. Soc.* **2017,** *139* (34), 11678-11681.

31. Lim, J.; Shin, H.; Kim, M.; Lee, H.; Lee, K. S.; Kwon, Y.; Song, D.; Oh, S.; Kim, H.; Cho, E. Ga-Doped Pt-Ni Octahedral Nanoparticles as a Highly Active and Durable Electrocatalyst for Oxygen Reduction Reaction. *Nano Lett.* **2018,** *18* (4), 2450-2458.

32. Dionigi, F.; Weber, C. C.; Primbs, M.; Gocyla, M.; Bonastre, A. M.; Spori, C.; Schmies, H.; Hornberger, E.; Kuhl, S.; Drnec, J.; Heggen, M.; Sharman, J.; Dunin-Borkowski, R. E.; Strasser, P. Controlling Near-Surface Ni Composition in Octahedral PtNi(Mo) Nanoparticles by Mo Doping for a Highly Active Oxygen Reduction Reaction Catalyst. *Nano Lett.* **2019,** *19* (10), 6876-6885.

33. Jia, Q.; Zhao, Z.; Cao, L.; Li, J.; Ghoshal, S.; Davies, V.; Stavitski, E.; Attenkofer, K.; Liu, Z.; Li, M.; Duan, X.; Mukerjee, S.; Mueller, T.; Huang, Y. Roles of Mo Surface Dopants in Enhancing the ORR Performance of Octahedral PtNi Nanoparticles. *Nano Lett.* **2018,** *18* (2), 798-804.

34. Wang, C.; Zhang, L.; Yang, H.; Pan, J.; Liu, J.; Dotse, C.; Luan, Y.; Gao, R.; Lin, C.; Zhang, J.; Kilcrease, J. P.; Wen, X.; Zou, S.; Fang, J. High-Indexed Pt_3Ni Alloy Tetrahexahedral Nanoframes Evolved through Preferential CO Etching. *Nano Lett.* **2017,** *17* (4), 2204-2210.

35. Wang, C.; Lin, C.; Zhao, B.; Zhang, L.; Kumbhar, A.; Fan, G.; Sun, K.; Zhang, J.; Chen, S.; Fang, J. High-Indexed Pt_3Fe Nanocatalysts and Their Enhanced Catalytic Performance in Dual Organic Reactions. *ChemNanoMat* **2015,** *1* (5), 331-337.

36. Cheng, T.; Goddard, W. A.; An, Q.; Xiao, H.; Merinov, B.; Morozov, S. Mechanism and Kinetics of the Electrocatalytic Reaction Responsible for the High Cost of Hydrogen Fuel Cells. *PCCP* **2017,** *19* (4), 2666-2673.

Supporting Information

Enhanced Oxygen Reduction Performance on {101} $CoMn_2O_4$ Spinel Facets

Ming Zhou,[†,§] Dasol Yoon,[∥,‡,§] Yao Yang,[⊥,§] Lihua Zhang,[▽] Can Li,[†] Hongsen Wang,[⊥] Anju Sharma,[#] Shaojie Jiang,[†] David A. Muller,[*,∥] Héctor D. Abruña,[*,⊥] and Jiye Fang[*,†]

[†]Department of Chemistry, State University of New York at Binghamton, Binghamton, New York 13902, United States;
[∥]School of Applied and Engineering Physics, Cornell University, Ithaca, New York 14853, United States;
[‡]Department of Materials Science and Engineering, Cornell University, Ithaca, New York 14853, United States;
[⊥]Department of Chemistry and Chemical Biology, Cornell University, Ithaca, New York 14853, United States;
[▽]Center for Functional Nanomaterials, Brookhaven National Laboratory, Upton, New York 11973, United States;
[#]Analytical and Diagnostics Lab, State University of New York at Binghamton, Binghamton, New York 13902, United States.

*Corresponding authors.

[§] These authors contributed equally to this work.

1. Experimental Section

Chemicals: Cobalt(II) chloride hexahydrate ($CoCl_2 \cdot 6H_2O$, 98%), manganese(II) acetate tetrahydrate ($Mn(OAc)_2 \cdot 4H_2O$, 98%), cobalt acetylacetonate ($Co(acac)_2$, ≥97%), oleylamine (OAm, 70%), oleic acid (OA, 90%), xylenes (≥98%), anhydrou hexane (≥98.5%), potassium hydroxide (KOH, ≥99.95%), 5% Nafion and isopropanol (anhydrous, 99.5%) were purchased from MilliporeSigma and used as received without further purification. Anhydrous ethanol (200 proof) was obtained from PHARMCO. Ketjen Black carbon powder EC600JD was provided by AkzoNobel. Deionized (DI) water with a resistivity of 18.2 MΩ·cm was obtained from a Purelab Flex3 water purification system (ELGA, UK).

Colloidal Synthesis of $CoMn_2O_4$ Spinel Nano-octahedra and Nanospheres: $CoMn_2O_4$ spinel nano-octahedra were prepared using a one-pot approach. In a standard synthesis, 20.0 mg of $CoCl_2 \cdot 6H_2O$, 40.0 mg of $Mn(OAc)_2 \cdot 4H_2O$, 2.6 mL of OAm, 1.3 mL of OA, and 6.0 mL of xylene were combined in a 100 ml three-neck flask in an air atmosphere. The as-prepared mixture was sonicated for 5 min at room temperature to help dissolve all the solids completely and then heated to 90 °C at 5 °C/min under vigorous magnetic stirring. After 20 min, 1.0 mL of DI water was rapidly injected into the aforementioned mixture with a syringe, accompanying a rapid color change in the solution from brown to dark violet, implying the quick formation of bimetallic Co-Mn hydroxides as the intermediate species for the sequent conversion into the $CoMn_2O_4$ spinels. Subsequently, the resultant solution was aged at 90 °C for 24 h, followed by natural cooling down to room temperature. Finally, the products were precipitated using 5.0 ml of hexane and 15.0 ml of ethanol and centrifugation at 9 000 rpm for 10 min. They were further washed twice using a mixture of hexane and ethanol (1:2 in vol.) followed by centrifugation at 9 000 rpm for 10 min. The final product was re-dispersed in 5.0 ml of hexane for future use. For the synthesis of $CoMn_2O_4$ spinel nanospheres, the protocol was the same as that for the synthesis of $CoMn_2O_4$ spinel nano-octahedra, except for the addition of 29.9 mg of $Co(acac)_2$ instead of $CoCl_2 \cdot 6H_2O$.

Characterizations: X-ray diffraction (XRD) patterns were collected at a scan rate of 2° min^{-1} at 0.02° steps from 25 to 75° on a Rigaku Ultima IV Diffractometer. Pawley fitting was carried out using Topas (version 3) software package (1999 - 2000 Bruker AXS). X-ray photoelectron spectroscopy (XPS) spectra were acquired on a PHI 5000 Versaprobe scanning ESCA system from Physical Electronics, Inc. Monochromatic Al Kα X-rays of 1486.6 eV were employed with the spot size of 200 μm at 50 W. Pass energies of 117 eV and 23.5 eV were used to collect survey and region scans respectively. Data were acquired at the takeoff angle of 45°. Transmission electron microscopy (TEM) and High-resolution TEM (HRTEM) images were taken using JEOL JEM-2100F (Japan) operated at 200 kV. The samples for TEM and HRTEM characterizations were prepared by drop-casting the nanocrystal dispersions in hexane on amorphous carbon-coated Cu grids and drying under ambient conditions. Scanning transmission electron microscopy (STEM) images and elemental electron energy loss spectroscopy (EELS) maps were taken on a fifth-order aberration-corrected STEM (Cornell Nion UltraSTEM) operated at 100 kV with a sub-Ångström spatial resolution. EDX analysis together with partial STEM images was performed in STEM mode using an aberration-corrected JEOL 2200FS electron microscope equipped with a Bruker-AXS SDD detector and an FEI Talos 200X. The metal contents were measured using inductively coupled plasma-optical emission spectroscopy (ICP-OES, Optima 7000 DV).

Preparation of the Working Electrodes: The as-synthesized $CoMn_2O_4$ spinel nano-octahedra or nano-spheres were loaded onto carbon support (Ketjen Black EC600JD) with a metal oxide content

of 40%. Briefly, 5.0 mg of the $CoMn_2O_4$ spinel nanocrystals and 7.5 mg of Ketjen Black were mixed in 6.0 mL of ethanol under continuous ultrasonication for 2 h and collected by centrifugation at 9 000 rpm for 10 min. The carbon-supported $CoMn_2O_4$ spinel nanocrystals were then washed with 0.1 M KOH in ethanol solution and collected by centrifugation at 9 000 rpm for 10 min three times. The KOH-treated sample was further annealed in air at 300 °C for 12 h to help remove the surfactants adsorbed on the surface of the nanocrystals. Subsequently, 5.0 mg of the catalyst was redispersed in a mixture of 0.6 mL of DI water, 0.4 mL of isopropanol, and 10.0 μL of 5% Nafion under ultrasonication for 1 h. Finally, 10.0 μL of the suspension was placed on a pre-cleaned glassy carbon rotating disk electrode (RDE) from Pine Research Instrumentation (0.196 cm^2 in geometric area) and dried under ambient conditions at room temperature. Similarly, the Pt/C catalyst containing 20 wt % Pt supported on Vulcan XC-72R (from the Fuel Cells Store) was used as a benchmark for comparison. The Pt/C catalyst ink was produced by dispersing 2.0 mg of the Pt/C catalyst in a mixture containing 1.0 mL of isopropanol, 1.0 mL of DI water, and 20.0 μL of 5% Nafion under ultrasonication for ~1 h. Then, 5.0 μL of the Pt/C catalyst ink was loaded on a pre-cleaned glassy carbon RDE, and dried under ambient conditions at room temperature.

Electrochemical Measurements: All electrochemical measurements were carried out in a three-electrode cell using an electrochemical workstation (Gamry, 1000E) at room temperature (~25 ^oC). A glassy carbon electrode (GCE) with a diameter of 5 mm coated with catalysts was used as the working electrode. A Ag/AgCl in saturated KCl solution and a graphite rod were used as the reference and counter electrodes, respectively. The measurement system was also corrected with a hydrogen standard electrode (HydroFlex® Complete Package, gaskatel). All potentials were converted to the reversible hydrogen electrode (RHE), or V_{RHE}, by following the equation: E(RHE) = E(Ag/AgCl) + 1.0258 (V). Before electrochemical tests, the three-neck electrochemical cell was washed using aqua regia and then rinsed thoroughly using DI water to avoid any potential contamination of precious metals. The working electrodes were initially cycled between 0.1 and 1.42 V at 50 mV s^{-1} in Ar-saturated 1 M KOH for 50 cycles to remove the remained ligands on the catalyst surfaces and yield stable cyclic voltammetric (CV) profiles. The working electrodes were scanned between 0.38 and 1.09 V at 5 mV s^{-1} and 1 600 rpm in O_2-saturated 1 M KOH. It should be pointed out that the capacitive background currents in CV curves, measured in Ar-saturated 1 M KOH solution were subtracted from the raw ORR data. Durability tests were carried out by potential cycling from 0.6 V to 1.0 V at 100 mV s^{-1} for 10 000 cycles. To avoid potential contamination from metal species dissolved in the solution, the oxygen reduction reaction (ORR) profiles after 10 000 cycles were obtained in a fresh O_2-saturated 1 M KOH solution. All the aforementioned results were obtained based on the measurements of more than 3 electrodes made of each sample.

TEM Sample Preparation after the Accelerated Durability Tests (ADTs): Following the ADTs, the electrode coated with the catalyst was immersed in a limited amount of anhydrous ethanol and sonicated. The resulting catalyst suspension was then precipitated through high-speed centrifugation (12 000 rpm for 5 min) and re-dispersed in ethanol for two cycles. To ensure the complete removal of any residue from the Nafion binder, the collected catalyst underwent multiple thorough washes with ethanol before TEM sample preparation for HRTEM/HAADF-STEM imaging and EDX mapping.

2. Supplemental Table and Figures

Table S1. Mass activity summary of some Co-, Mn-based spinel electrocatalysts towards ORR in alkaline media.

Catalysts	Electrolyte	Mass activity ($A\ g^{-1}$)	Reference
$CoMn_2O_4$ nano-octahedra	O_2-saturated 1 M KOH	60.0@0.85 V	**This work**
$CoMn_2O_4$ nanospheres		38.6@0.85 V	
$CoMn_2O_4$ nanoparticles	O_2-saturated 1 M KOH	31@0.85 V	*Ref.*[1]
Co_3O_4 nanoparticles		27@0.85 V	
$CoFe_2O_4$ nanoparticles		18@0.85 V	
Mn_3O_4 nanoparticles		13@0.85 V	
Co_2VO_4 nanosheets	O_2-saturated 1 M KOH	5.2@0.85 V	*Ref.*[2]
$MnCo_2O_4$ spinels	O_2-saturated 0.1 M KOH	10.0@0.85 V	*Ref.*[3]
$Mn_{0.8}(CoFe_2)_{0.73}O_4$ nanoparticles	O_2-saturated 1 M NaOH	7.25@0.85 V	*Ref.*[4]
$Co_{1.5}Mn_{1.5}O_4$/C	O_2-saturated 1 M KOH	28.41@0.85 V	*Ref.*[5]
$CoMn_2O_4$/nitrogen-doped carbon nanofibers	O_2-saturated 0.1 M KOH	34.2@0.85 V	*Ref.*[6]
$Co_{0.25}Mn_{0.75}Fe_{2.0}$ multi-metal oxide nanoparticles	O_2-saturated 1 M KOH	46.9@0.9 V	*Ref.*[7]
mesostructured $CuCo_2O_4$	O_2-saturated 0.1 M KOH	16.4@0.9 V	*Ref.*[8]
$ZnCo_2O_4$ microspheres	O_2-saturated 1 M KOH	2.8@0.85 V	*Ref.*[9]
$CuMn_2O_4$ nano-octahedra	O_2-saturated 1 M KOH	37.6@0.85 V	*Ref.*[10]
$MnCo_2O_4$ hollow mesoporous nanowires	O_2-saturated 0.1 M KOH	8.5@0.85 V	*Ref.*[11]

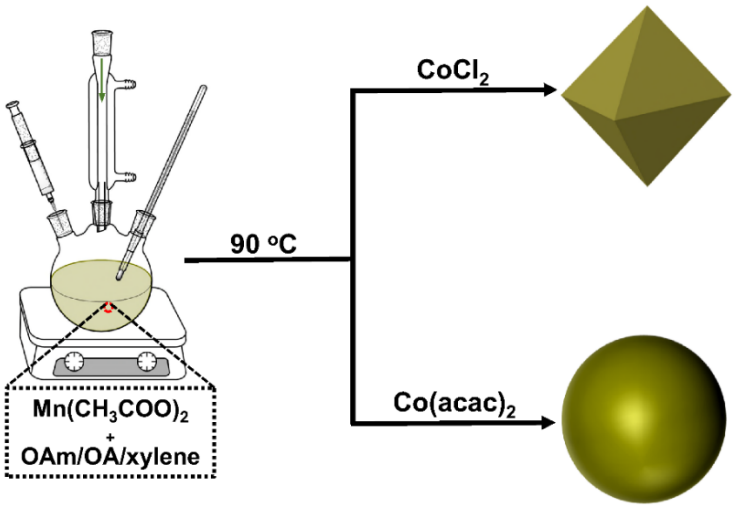

Figure S1. Schematic illustration of the syntheses of $CoMn_2O_4$ nano-octahedra and nanospheres.

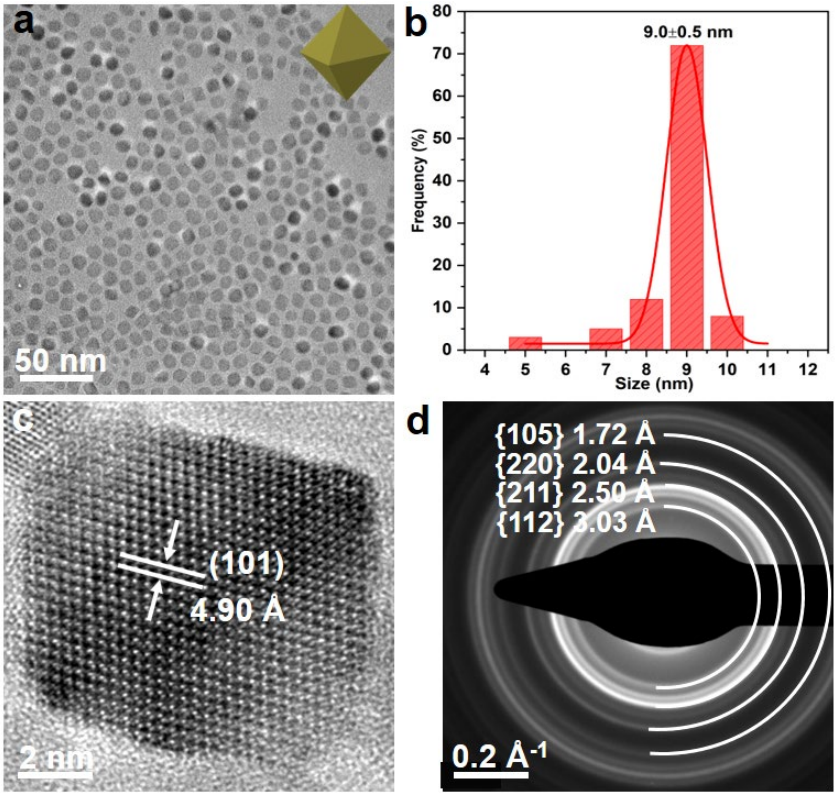

Figure S2. (a) Low-magnification TEM image of the as-prepared $CoMn_2O_4$ nano-octahedra. (b) Size distribution histogram of the $CoMn_2O_4$ nano-octahedra. (c) HRTEM image of a representative $CoMn_2O_4$ nano-octahedron. (d) SAED pattern of the $CoMn_2O_4$ nano-octahedra. The inset in (a) displays the 3D model of the octahedral nanocrystals corresponding to the TEM image.

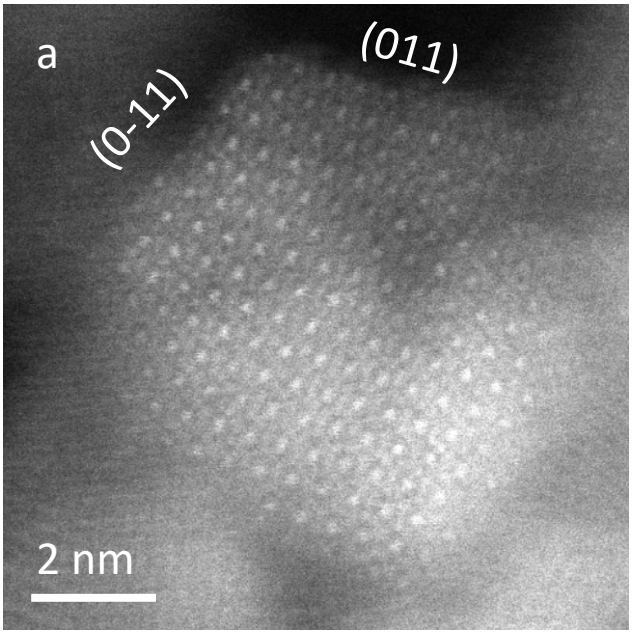

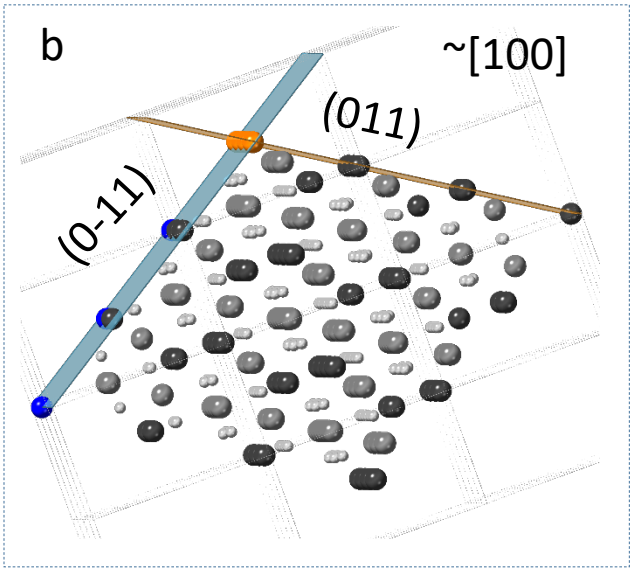

Figure S3. (a) HAADF-STEM image of the as-prepared $CoMn_2O_4$ nano-octahedron viewed down in [100]. The edges are perpendicular to {101} facets. (b) Structural model of the $CoMn_2O_4$ nano-octahedron, slightly tilted from [100] to show {101} planes.

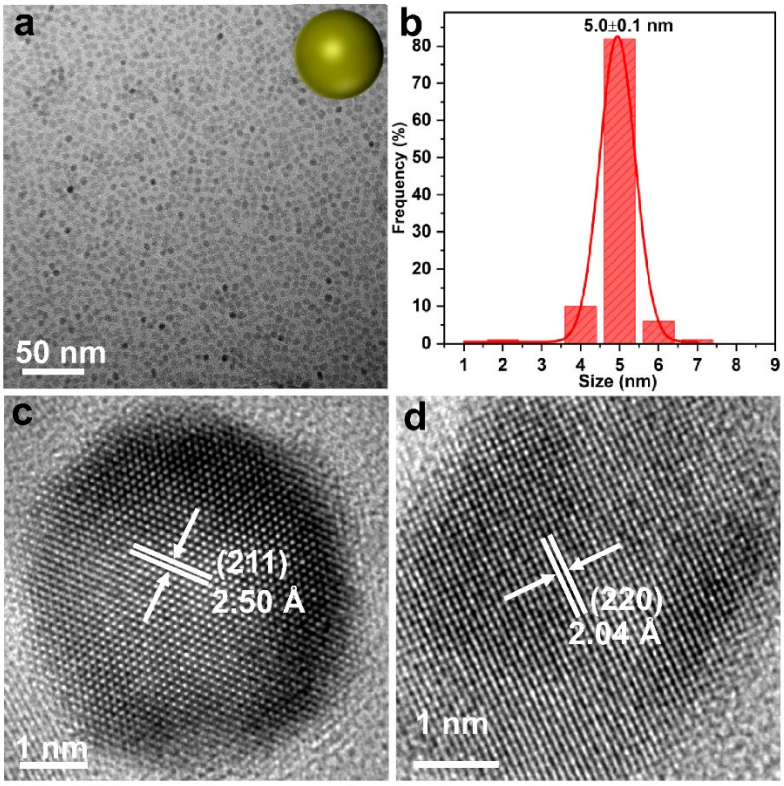

Figure S4. (a) Low-magnification TEM image of the as-prepared $CoMn_2O_4$ nanospheres. (b) Size distribution histogram of the $CoMn_2O_4$ nanospheres. (c, d) HRTEM images of a representative $CoMn_2O_4$ nanosphere. The inset in (a) displays the 3D model of the spherical nanocrystals corresponding to the TEM image.

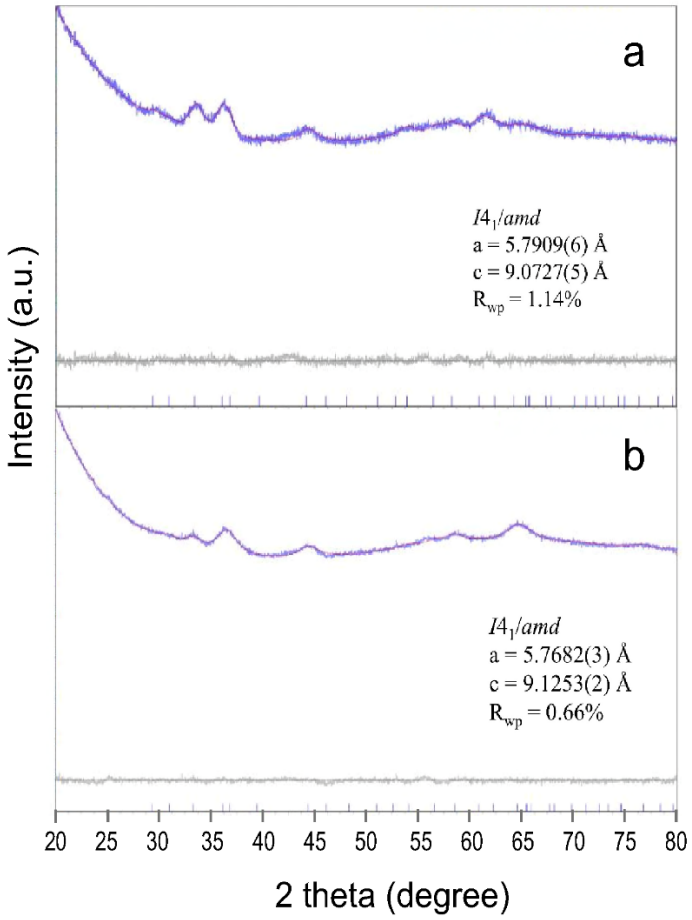

Figure S5. Lattice parameters of carbon-supported (Ketjen Black EC-600JD) $CoMn_2O_4$ nano-octahedra received from Pawley fitting. "R_{wp}" means the weighted profile R-factor.[12] (a), as-synthesized $CoMn_2O_4$ nano-octahedra. (b) $CoMn_2O_4$ nano-octahedra annealed in air at 300 °C for 12 h. The cell parameters *a* and *c* in a standard JCPDS card (No. 77-0471) are 5.784 Å and 9.091 Å, respectively.

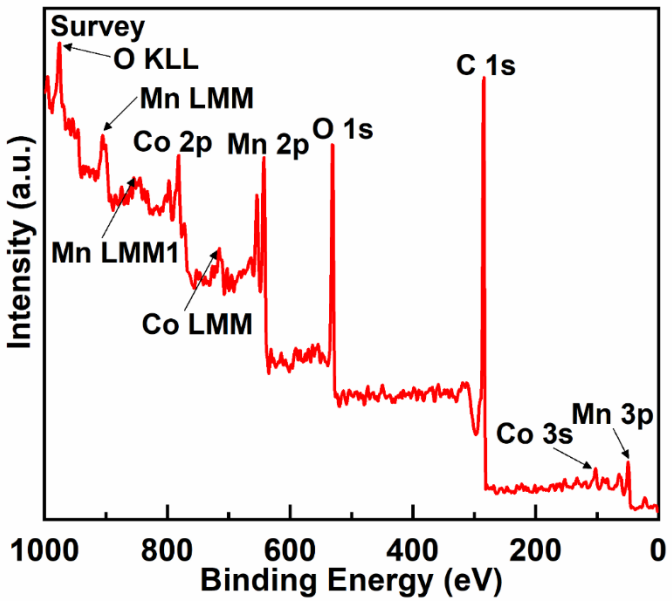

Figure S6. XPS survey spectrum of $CoMn_2O_4$ nano-octahedra after annealing in air at 300 °C for 12 h.

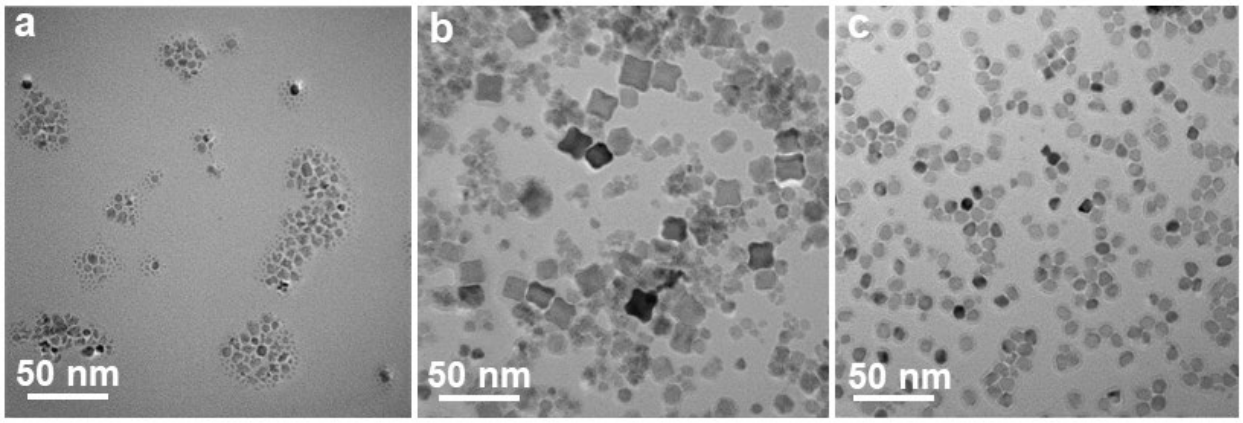

Figure S7. TEM images of the nanocrystals synthesized under the same conditions, except that (a) no oleic acid was added to the reaction solution; (b) $Co(acac)_2$ was replaced with $CoBr_2$; (c) half amount of water was added into the reaction system.

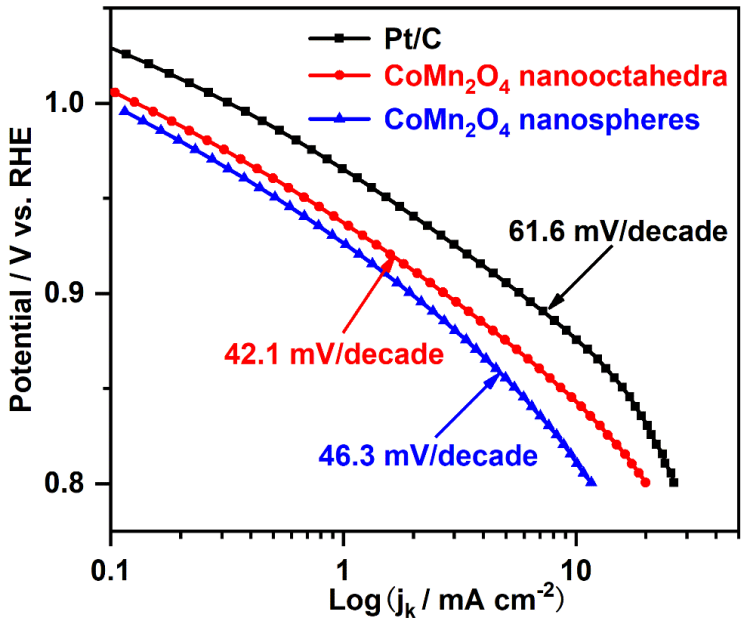

Figure S8. Tafel plots derived from the ORR polarization profiles of $CoMn_2O_4$ nano-octahedra, $CoMn_2O_4$ nanospheres, and Pt/C, in Figure 3a. Spinel samples were annealed in air at 300 ºC for 12 h. Note that Tafel slopes are shown on the plot.

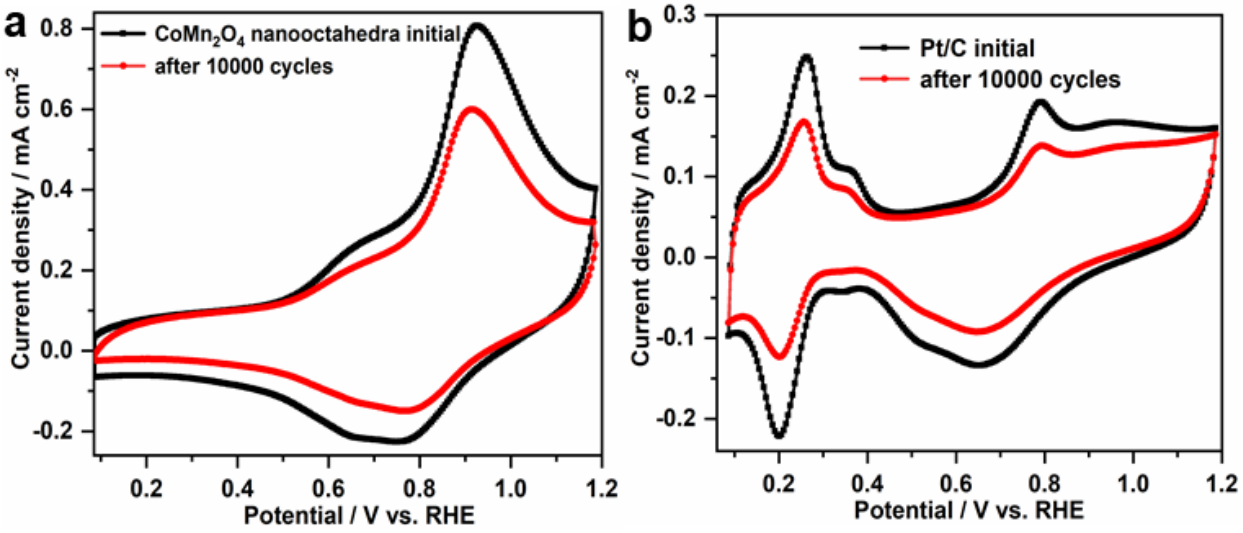

Figure S9. CV curves of (a) $CoMn_2O_4$ nano-octahedra (annealed in air at 300 ºC for 12 h) and (b) Pt/C at a scan rate of 5 mV/s at 1 600 rpm. The accelerated durability tests were performed in O_2-saturated 1 M KOH at a scan rate of 100 mV/s from 0.6 to 1.0 V *vs.* RHE.

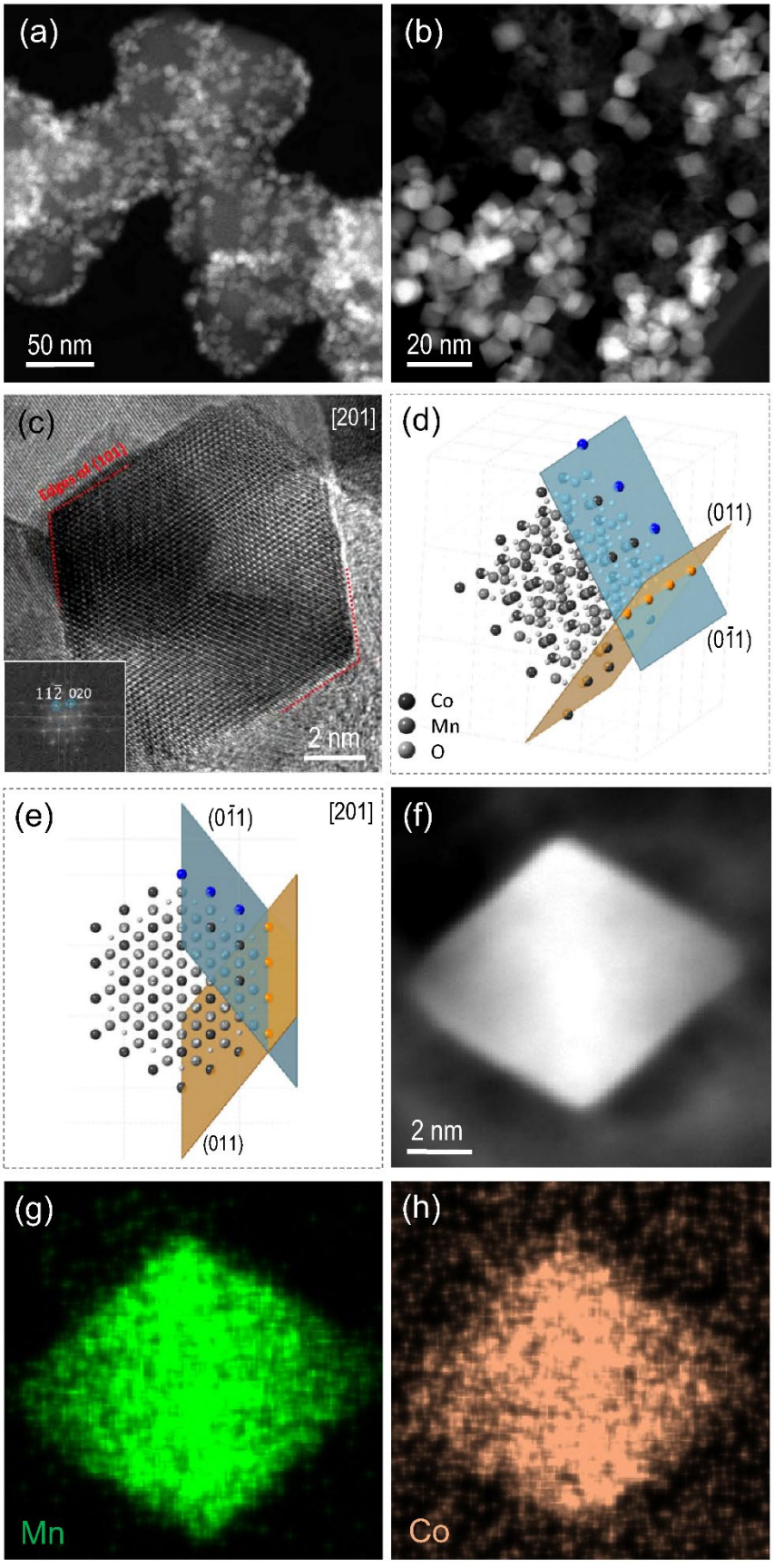
(a)
50 nm
(b)
20 nm
(c)
[201]
Edges of {101}
11$\bar{2}$ 020
2 nm
(d)
(011)
(0$\bar{1}$1)
Co
Mn
O
(e)
(0$\bar{1}$1)
[201]
(011)
(f)
2 nm
(g)
Mn
(h)
Co

Figure S10. (a) Low-magnification and (b) High-magnification HAADF-STEM images of the carbon-supported $CoMn_2O_4$ nano-octahedra after the accelerated durability test. (c) HRTEM image taken from an individual $CoMn_2O_4$ nano-octahedron supported by carbon black after the accelerated durability test along the [201] zone axis. The inset in (c) is a diffractogram obtained from a fast Fourier transform of this image. (d) Structural model of $CoMn_2O_4$ nano-octahedron with (011) and $(0\bar{1}1)$ planes highlighted in orange and blue colors, respectively. Some atoms on the edges of the {101} facets are colored in orange and blue as a visual guide. (e) A structural model viewed down in [201]. The edges intersect with {101} planes. (f) STEM image and (g, h) the corresponding EDX elemental mappings of a representative carbon-supported $CoMn_2O_4$ nano-octahedron after the accelerated durability test.

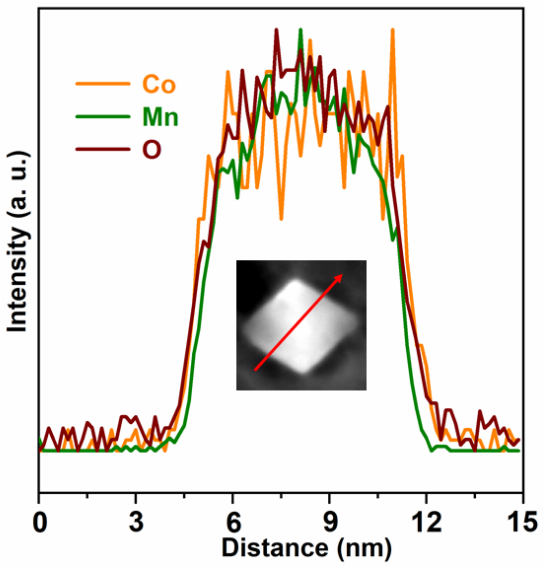

Figure S11. Normalized EDX line scan across an individual carbon-supported $CoMn_2O_4$ nano-octahedron after the accelerated durability tests.

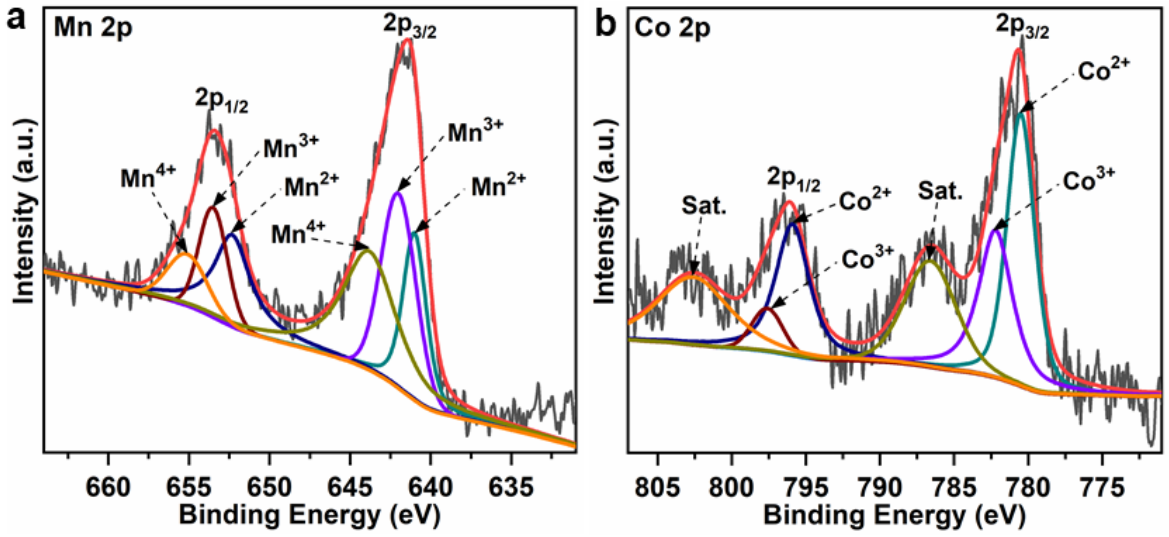

Figure S12. XPS spectra of (a) Mn *2p* and (b) Co *2p* for carbon-supported $CoMn_2O_4$ nano-octahedra after the accelerated durability test. Ratios of element states: $Mn^{2+}/Mn^{3+}/Mn^{4+}$ = 23/62 /15; Co^{2+}/Co^{3+} = 70:30.

3. References:

1. Yang, Y.; Xiong, Y.; Holtz, M. E.; Feng, X.; Zeng, R.; Chen, G.; DiSalvo, F. J.; Muller, D. A.; Abruña, H. D. Octahedral Spinel Electrocatalysts for Alkaline Fuel Cells. *Proc. Natl. Acad. Sci.* **2019,** *116* (49), 24425-24432.

2. Mu, C.; Mao, J.; Guo, J.; Guo, Q.; Li, Z.; Qin, W.; Hu, Z.; Davey, K.; Ling, T.; Qiao, S.-Z. Rational Design of Spinel Cobalt Vanadate Oxide Co_2VO_4 for Superior Electrocatalysis. *Adv. Mater.* **2020,** *32* (10), 1907168.

3. Wei, C.; Feng, Z.; Scherer, G. G.; Barber, J.; Shao-Horn, Y.; Xu, Z. J. Cations in Octahedral Sites: A Descriptor for Oxygen Electrocatalysis on Transition-Metal Spinels. *Adv. Mater.* **2017,** *29* (23), 1606800.

4. Xiong, Y.; Yang, Y.; Feng, X.; DiSalvo, F. J.; Abruña, H. D. A Strategy for Increasing the Efficiency of the Oxygen Reduction Reaction in Mn-Doped Cobalt Ferrites. *J. Am. Chem. Soc.* **2019,** *141* (10), 4412-4421.

5. Yang, Y.; Wang, Y.; Xiong, Y.; Huang, X.; Shen, L.; Huang, R.; Wang, H.; Pastore, J. P.; Yu, S.-H.; Xiao, L.; Brock, J. D.; Zhuang, L.; Abruña, H. D. In Situ X-ray Absorption Spectroscopy of a Synergistic Co–Mn Oxide Catalyst for the Oxygen Reduction Reaction. *J. Am. Chem. Soc.* **2019,** *141* (4), 1463-1466.

6. Chen, X.; Yan, Z.; Yu, M.; Sun, H.; Liu, F.; Zhang, Q.; Cheng, F.; Chen, J. Spinel Oxide Nanoparticles Embedded in Nitrogen-Doped Carbon Nanofibers as A Robust and Self-Standing Bifunctional Oxygen Cathode for Zn-Air Batteries. *J. Mater. Chem. A* **2019,** *7* (43), 24868-24876.

7. Kim, J.; Ko, W.; Yoo, J. M.; Paidi, V. K.; Jang, H. Y.; Shepit, M.; Lee, J.; Chang, H.; Lee, H. S.; Jo, J.; Kim, B. H.; Cho, S.-P.; van Lierop, J.; Kim, D.; Lee, K.-S.; Back, S.; Sung, Y.-E.; Hyeon, T. Structural Insights into Multi-Metal Spinel Oxide Nanoparticles for Boosting Oxygen Reduction Electrocatalysis. *Adv. Mater.* **2022,** *34* (8), 2107868.

8. Behnken, J.; Yu, M.; Deng, X.; Tüysüz, H.; Harms, C.; Dyck, A.; Wittstock, G. Oxygen Reduction Reaction Activity of Mesostructured Cobalt-Based Metal Oxides Studied with the Cavity-Microelectrode Technique. *ChemElectroChem* **2019,** *6* (13), 3460-3467.

9. Chakrabarty, S.; Mukherjee, A.; Su, W.-N.; Basu, S. Improved Bi-Functional ORR and OER Catalytic Activity of Reduced Graphene Oxide Supported $ZnCo_2O_4$ Microsphere. *Int. J. Hydrogen Energy* **2019,** *44* (3), 1565-1578.

10. Zhou, M.; Wang, H.; Zhang, L.; Li, C.; Kumbhar, A.; Abruña, H. D.; Fang, J. Facet Impact of $CuMn_2O_4$ Spinel Nanocatalysts on Enhancement of the Oxygen Reduction Reaction in Alkaline Media. *ACS Catal.* **2022,** *12* (21), 13663-13670.

11. An, L.; Hu, Y.; Li, J.; Zhu, J.; Sun, M.; Huang, B.; Xi, P.; Yan, C.-H. Tailoring Oxygen Reduction Reaction Pathway on Spinel Oxides via Surficial Geometrical-Site Occupation Modification Driven by the Oxygen Evolution Reaction. *Adv. Mater.* **2022,** *34* (28), 2202874.

12. Toby, B. H. R Factors in Rietveld Analysis: How Good Is Good Enough? *Powder Diffr.* **2006,** *21* (1), 67-70.